Monthly Notices of the ROYAL ASTRONOMICAL SOCIETY
MNRAS **517,** 2990–3007 (2022) https://doi.org/10.1093/mnras/stac2514

Cloud-scale radio surveys of star formation and feedback in Triangulum Galaxy M 33: VLA observations

F. S. Tabatabaei [1,2,3,4]★ W. Cotton,[5] E. Schinnerer,[3] R. Beck,[4] A. Brunthaler,[4] K. M. Menten,[4] J. Braine,[6] E. Corbelli,[7] C. Kramer,[8] J. E. Beckman,[2,9] J. H. Knapen,[2,9] R. Paladino,[10] E. Koch [11] and A. Camps Fariña[2,9,12]

[1]*School of Astronomy, Institute for Research in Fundamental Sciences (IPM), PO Box 19395-5531 Tehran, Iran*
[2]*Instituto de Astrofísica de Canarias, Vía Láctea S/N, E-38205 La Laguna, Spain*
[3]*Max-Planck-Institut für Astronomie, Königstuhl 17, D-69117, Heidelberg, Germany*
[4]*Max-Planck Institut für Radioastronomie, Auf dem Hügel 69, D-53121 Bonn, Germany*
[5]*National Radio Astronomy Observatory (NRAO), 520 Edgemont Road, Charlottesville, VA 22903, USA*
[6]*Laboratoire d'Astrophysique de Bordeaux, Univ. Bordeaux, CNRS, B18N, Allée Geoffroy Saint-Hilaire, F-33615 Pessac, France*
[7]*INAF – Osservatorio Astrofisico di Arcetri, Largo E. Fermi, 5, I-50125 Firenze, Italy*
[8]*Institut de Radioastronomie Millimétrique (IRAM), 300 Rue de la Piscine, F-38406 Saint Martin d'Hères, France*
[9]*Departamento de Astrofísica, Universidad de La Laguna, E-38206 La Laguna, Spain*
[10]*INAF – Istituto di Radioastronomia, via P. Gobetti 101, I-40129 Bologna, Italy*
[11]*Center for Astrophysics, Harvard & Smithsonian, 60 Garden St., Cambridge, MA 02138, USA*
[12]*Departamento de la Tierra y Astrofísica, Facultad de CC Físicas, Universidad Complutense de Madrid, E-28040 Madrid, Spain*

Accepted 2022 August 28. Received 2022 August 28; in original form 2022 March 15

ABSTRACT

Studying the interplay between massive star formation and the interstellar medium (ISM) is paramount to understand the evolution of galaxies. Radio continuum (RC) emission serves as an extinction-free tracer of both massive star formation and the energetic components of the ISM. We present a multiband RC survey of the Local Group galaxy M 33 down to $\simeq$30 pc linear resolution observed with the Karl G. Jansky *Very Large Array (VLA)*. We calibrate the star formation rate surface density and investigate the impact of diffuse emission on this calibration using a structural decomposition. Separating the thermal and non-thermal emission components, the correlation between different phases of the ISM, and the impact of massive star formation are being investigated. Radio sources with sizes $\lesssim$200 pc constitute about 36 per cent (46 per cent) of the total RC emission at 1.5 GHz (6.3 GHz) in the inner 18 × 18 arcmin^2 (or 4 kpc × 4 kpc) disc of M 33. The non-thermal spectral index becomes flatter with increasing star formation rate surface density, indicating the escape of cosmic ray electrons from their birth places. The magnetic field strength also increases with star formation rate following a bi-modal relation, indicating that the small-scale turbulent dynamo acts more efficiently at higher luminosities and star formation rates. Although the correlations are tighter in star-forming regions, the non-thermal emission is also correlated with the more quiescent molecular gas in the ISM. An almost linear molecular star formation law exists in M 33 when excluding diffuse structures. Massive star formation amplifies the magnetic field and increases the number of high-energy cosmic ray electrons, which can help the onset of winds and outflows.

Key words: radiation mechanisms: non-thermal – ISM: magnetic fields – (ISM:) cosmic rays – galaxies: individual: M 33 – galaxies: star formation – radio continuum: ISM.

1 INTRODUCTION

The RC emission from galaxies is mainly linked to their massive star formation and nuclear activity (e.g. Condon 1992). Massive stars produce RC emission while in their early phases of evolution [young stellar objects (YSOs) such as protostars with radio jets/outflows and young O and early B-type stars creating H II regions] and in their late phases of evolution (supernova explosions, SNe, and supernova remnants, SNRs). Hence, being dust-unbiased, RC surveys are ideal tools to trace different evolutionary phases of massive stars. Apart from tracing these stars, the way they interact with the interstellar medium (ISM) and the role of the ISM in the star formation process are key questions that address the evolution of galaxies (Tabatabaei et al. 2018). Resolved and sensitive RC observations of nearby galaxies exhibit extended structures besides bright star-forming regions, indicative of the diffuse ionized, magnetized, and relativistic ISM (e.g. Beck 2015; For et al. 2018; Krause et al. 2018). These RC maps are ideal to address the effect of massive star formation on the ISM and vice versa.

A careful separation of the thermal (TH) and non-thermal (NTH) RC components in galaxies shows that the cosmic ray electrons (CRes), which have a relatively flat power-law spectral index, are more energetic in complexes of star-forming regions, where the

★ E-mail: fatemeht@gmail.com, ftaba@ipm.ir

magnetic field is also stronger (Tabatabaei et al. 2007c, 2013a; Hassani et al. 2022). Hence, massive star formation can insert strong NTH pressure into the ISM through injection of CRes and the amplification of magnetic fields, besides their TH feedback. This can cause cosmic ray-driven winds and outflows in galaxies (Tabatabaei et al. 2017). Understanding the formation of the next generation of stars in such a magnetized and turbulent ISM is a pressing question. Sensitive RC observations on cloud scales in nearby galaxies are vital to study the formation and regulation of stars in the presence of magnetic fields and cosmic rays.

In normal star-forming galaxies, a linear correlation is expected between the star formation rate (SFR) and the RC emission if the production rate of CRes, assumed to be proportional to the SNe rate, is proportional to the SFR and if CRes lose their energy before escaping from a galaxy (Völk 1989; Condon 1992). A detailed study of the mid-radio wavelength spectral energy distribution (1–10 GHz SED) showed that while the correlation is linear with the TH component, it deviates from linearity for the NTH component (galaxies with higher SFR are brighter in NTH RC, Tabatabaei et al. 2017). A similar deviation from linearity had also been reported in integrated studies (e.g. Price & Duric 1992; Niklas 1997; Gürkan et al. 2018; Smith et al. 2021). This can be expected as the synchrotron emission depends not only on the CRe number but also the magnetic field strength. Galaxies with higher SFR also have stronger magnetic fields (e.g. Chyży et al. 2011; Heesen et al. 2014; Tabatabaei et al. 2017), likely due to feedback from star formation (Schleicher & Beck 2013). To understand the origin of this non-linearity, it is hence vital to resolve details of the connection of SFR with both the CRes (number and energy) and the magnetic field (strength and structure).

Studies of the RC correlation with the SFR surface density ($\Sigma_{\rm SFR}$) or the resolved RC–IR correlation show that different relations hold depending on galactic region, e.g. star-forming versus non-star-forming (Tabatabaei et al. 2013a) or spiral arms versus inter-arm regions (Dumas et al. 2011), and also on spatial scales (e.g. Tabatabaei et al. 2013b). Taking all structures together, Heesen et al. (2014) found a sublinear RC versus $\Sigma_{\rm SFR}$ relation (or superlinear $\Sigma_{\rm SFR}$ versus RC) in a number of galaxies studied in the SIRTF Nearby Galaxies Survey (SINGS; Kennicutt et al. 2003), concluding that using the RC emission alone is not sufficient to measure $\Sigma_{\rm SFR}$ locally. However, averaging over different galactic structures can also impose a bias on the $\Sigma_{\rm SFR}$ measurements due to the inclusion of emission unrelated to the current star formation activity. Decomposition of emission emerging from different galactic components, such as star-forming regions, extended structures, and diffuse disc(+ halo), i.e. structural decomposition, can hence be important when measuring the SFR using resolved RC maps.

Due to its proximity (d =730 kpc, 1 arcsec $\simeq$ 4 pc; Freedman, Wilson & Madore 1991) and viewing angle (i = 56°; Regan & Vogel 1994), the Triangulum Galaxy M 33 (NGC 598, see Table 1 for general positional data) provides a unique laboratory to resolve the ISM structures and dominant processes in both star-forming and non-star-forming regions. Radio surveys of M 33 have mainly targeted large-scale ISM structures ($\gtrsim$1 kpc; Israel & van der Kruit 1974; von Kap-Herr, Berkhuijsen & Wielebinski 1978; Beck 1979; Buczilowski & Beck 1987) or bright sources such as H II regions and SNRs (Viallefond et al. 1986; Duric et al. 1993; White et al. 2019). In the latter surveys, the ISM adjacent to bright radio sources is usually neglected due to either insufficient sensitivity or the missing short spacing problem in radio interferometry. Recovering the short-spacing emission using an image reconstruction technique allowed Tabatabaei et al. (2007a, 2013b) and Tabatabaei, Krause & Beck (2007b) to study M 33's ISM structures down to 200-pc scales (50 arcsec). Here, we report a new wide-band, full polarization RC survey of M 33 with the *Karl G. Jansky Very Large Array* (VLA) at C (6.3 GHz central frequency) and L (1.5 GHz central frequency) bands. These observations allow us to study the ISM down to 30-pc scales, addressing not only star-forming regions but also the more quiescent, non-star-forming regions that are needed to investigate the regulation of star formation in this galaxy.

Table 1. Positional data on M 33.

Nucleus position (J2000)[1]	RA = $1^{\rm h}33^{\rm m}51\overset{\rm s}{.}0$
	DEC = $30°39'37\overset{''}{.}0$
Position angle of major axis[2]	23°
Inclination[3]	56°
Distance[4] (1 arcsec = 3.5 pc)	730 kpc

[1] de Vaucouleurs & Leach (1981)
[2] Deul & van der Hulst (1987)
[3] Regan & Vogel (1994)
[4] Brunthaler et al. (2005)

Taking advantage of the VLA's wide-bandwidth WIDAR correlator, we present resolved RC maps of M 33 at significantly higher sensitivity than before (Tabatabaei et al. 2007a, b). The VLA observations were designed to achieve a resolution similar to those of the IRAM 30m CO(2-1; Gratier et al. 2010; Druard et al. 2014) and the *Herschel PACS* continuum observations (Kramer et al. 2010; Boquien et al. 2015) to perform a consistent comparison of the various ISM phases and components.

Thanks to these high-resolution and -sensitivity data, this paper presents a study of (1) the effect of diffuse galactic components calibrating the $\Sigma_{\rm SFR}$, (2) the correlation between RC-emitting components and neutral gas phases of the ISM, and (3) the impact of massive star formation on relativistic and magnetized ISM.

The paper is organized as follows: After describing the observations and data in Section 2[1] and the TH/NTH separation method (Section 3), we present the resulting observations, as well as the TH and NTH maps, the spectral index, and equipartition magnetic field in Section 4. Then we discuss the SFR–RC calibrations, the RC–neutral gas correlations, and investigate the impact of star formation on CRes and magnetic fields (Section 5). Our findings are summarized in Section 6.

2 DATA

2.1 VLA observations and data reduction

We performed interferometer observations with the Karl G. Jansky VLA[2]. The VLA observations were taken using the wideband, spectral line correlator WIDAR in full polarization under proposal number 11B-145 (PI: F. Tabatabaei). The observations were carried out in D-configuration in December 2011 and C- configuration in April 2012 at C (5.5-7.5 GHz) and L (1-2 GHz) bands. The corresponding scheduling blocks (SBs) and dates of observations used in this study are listed in Table 2.

At C band, two continuous base-bands, each with eight sub-bands of 128 MHz width, were tuned to cover 5–5.9 and 6.7–7.6 GHz. These observations image the central 18 × 18 arcmin^2 area including the central extended region and the main spiral arms. As the primary

[1]The polarization study will be presented elsewhere.
[2]The *VLA* is a facility of the National Radio Astronomy Observatory (NRAO). The NRAO is operated by Associated Universities, Inc., under contract with the National Science Foundation.

Table 2. VLA observations, scheduling blocks (SBs), dates, and total observation times.

Band	SB ID	Observation date	Total time (h)
C	5145344	2011 December 05	5
C	5765541	2011 December 06	5
C	5758725	2011 December 12 and 13	5
C	5760250	2011 December 13 and 14	5
C	5767346	2011 December 17, 18, and 21	10
L	9644094	2012 April 21	5.5

beam full width at half-maximum of 6 arcmin (at 7.5 GHz) is much smaller than this area, we performed mosaicing. Following Condon et al. (1998), a distance between pointings of $\theta_{\rm pb}/\sqrt{2} \simeq 4'$was needed to cover this area to obtain a composite image with uniform sensitivity leading to a mosaic of 25 pointings (5 pointings along each RA and Dec.).

The L-band (1–2 GHz) observations were carried out in C configuration. We used two base-bands of 512 MHz at their default frequencies of 1.25 and 1.75 GHz, each with eight sub-bands of 64 MHz. A mosaic of nine pointings with a pointing separation of 20 arcmin covered a 50 × 50 arcmin^2 area. Table 3 lists the central positions of the pointings observed at C and L bands.

The sources 3C 48 and 3C 138 were observed for calibrating the flux density and polarization angle.

The data were processed in the OBIT package (Cotton 2008). Calibration used the standard VLA calibration pipeline procedure. Initial flagging used a comparison with running medians in time and frequency to detect outliers. The switched power system was used to determine short-term variations in the receiver gain. Then group delay, bandpass, and amplitude and phase calibration were determined using 3C 48. Outliers among the calibration solutions were used to flag the data. After further flagging in frequency using a running median, the calibration steps were repeated. Polarization calibration used 3C 48 and 3C 138 with the polarization model of Perley & Butler (2013). The non-linear fitting did not fix any of the instrumental polarization parameters.

Imaging of each pointing in Stokes I, Q, and U used the wideband OBIT imager MFImage (Cotton et al. 2018). Variations in sky brightness and antenna gain with frequency were accommodated using 5 per cent fractional bandwidth sub-bands that are imaged independently but deconvolved jointly. A multiresolution CLEAN (roughly 9, 31, and 57 arcsec) was used to recover a wide range of size scales. Then those pointings with a peak over 3 mJy beam^{-1} were also phase self-calibrated. The calibrator was imaged in the same way as the targets, which resulted in some imaging artefacts being incorporated into the self-calibration model (and preserved). Briggs Robust image weighting resulted in the beams of all pointings being about 9.″2 × 8.″8 in C band and 12.″7 × 12.″5 in L band. Each pointing image was then convolved to a circular beam before combination to get consistent resolution (9.″35 and 15″ in C- and L-band, respectively).

A mosaic of the field for each image plane and for each frequency sub-band and Stokes parameter was derived by the summation over overlapping pointing images:

$$M(x,y) = \frac{\sum_{i=1}^{n} A_i(x,y)\, I_i(x,y)}{\sum_{i=1}^{n} A_i^2(x,y)},$$

where $A_i(x, y)$ is the antenna gain of pointing i in direction (x, y), $I_i(x, y)$ is the pointing i pixel value interpolated to direction (x, y), and M is the mosaiced image.

Table 3. Central positions of the pointings observed with VLA at C (5–7.6 GHz) and L (1–2 GHz) bands.

Band	Pointing #	RA (J2000) ($^h\,^m\,^s$)	Dec. (J2000) ($^\circ\,'\,''$)
C	1	01^{h}34^{m}40.^{s}00	+30°48′5.″80
C	2	01^{h}34^{m}20.^{s}27	+30°48′5.″80
C	3	01^{h}34^{m}0.^{s}54	+30°48′5.″80
C	4	01^{h}33^{m}40.^{s}82	+30°48′5.″80
C	5	01^{h}33^{m}21.^{s}09	+30°48′5.″80
C	6	01^{h}34^{m}40.^{s}00	+30°43′51.″40
C	7	01^{h}34^{m}20.^{s}27	+30°43′51.″40
C	8	01^{h}34^{m}0.^{s}54	+30°43′51.″40
C	9	01^{h}33^{m}40.^{s}82	+30°43′51.″40
C	10	01^{h}33^{m}21.^{s}09	+30°43′51.″40
C	11	01^{h}34^{m}35.^{s}00	+30°39′37.″00
C	12	01^{h}34^{m}15.^{s}29	+30°39′37.″00
C	13	01^{h}33^{m}55.^{s}57	+30°39′37.″00
C	14	01^{h}33^{m}35.^{s}86	+30°39′37.″00
C	15	01^{h}33^{m}16.^{s}15	+30°39′37.″00
C	16	01^{h}34 34.^{s}00	+30°35′22.″60
C	17	01^{h}34^{m}14.^{s}30	+30°35′22.″60
C	18	01^{h}33^{m}54.^{s}60	+30°35′22.″60
C	19	01^{h}33^{m}34.^{s}90	+30°35′22.″60
C	20	01^{h}33^{m}15.^{s}20	+30°35′22.″60
C	21	01^{h}34^{m}30.^{s}00	+30°31′8.″20
C	22	01^{h}34^{m}10.^{s}31	+30°31′8.″20
C	23	01^{h}33^{m}50.^{s}63	+30°31′8.″20
C	24	01^{h}33^{m}30.^{s}95	+30°31′8.″20
C	25	01^{h}33^{m}11.^{s}26	+30°31′8.″20
L	1	01^{h}35^{m}11.^{s}00	+30°19′37.″00
L	2	01^{h}33^{m}51.^{s}00	+30°19′37.″00
L	3	01^{h}32^{m}31.^{s}00	+30°19′37.″00
L	4	01^{h}32^{m}31.^{s}00	+30°39′37.″00
L	5	01^{h}33^{m}51.^{s}00	+30°39′37.″00
L	6	01^{h}35^{m}11.^{s}00	+30°39′37.″00
L	7	01^{h}35^{m}11.^{s}00	+30°59′37.″00
L	8	01^{h}33^{m}51.^{s}00	+30°59′37.″00
L	9	01^{h}32^{m}31.^{s}00	+30°59′37.″00

The rms noise at each spectral window is given in Table 4. At C-band, combining the spectral window images led to a final rms noise of 6 μJy per 9.35 arcsec beamwidth at the central frequency of 6.3 GHz, which is close to the TH noise. Broad-band radio frequency interfence affected the L-band observations particularly at the sub-bands 1, 2, and 10, leading to relatively higher noise level (sub-band 10 was totally flagged). The rms noise of the combined L-band spectral windows is about 37 μJy per 15 arcsec beamwidth at 1.5 GHz.

2.2 Other data

To increase the image fidelity at 1.5 GHz, we also used the VLA L-band data taken in the D-configuration and presented by Tabatabaei et al. (2007b). The 100-m Effelsberg maps at 6 cm (Tabatabaei et al. 2007b) and 20 cm (Fletcher 2001) were used to correct for the missing short spacing of the VLA data.

Hα line emission was mapped with the 0.6 meter *Burrell–Schmidt telescope* at the Kitt Peak National Observatory by Hoopes & Walterbos (2000), covering a 68 × 68 arcmin^2 field of view. We corrected the data for the neighbouring N II line emission using

Table 4. Rms noise in the sub-band images at 9.35 arcsec (C-band) and 15 arcsec (L-band) resolutions.

Sub-band #	C-Band Central frequency (MHz)	rms noise (μJy/ beam)	L-Band Central frequency (MHz)	rms noise (μJy/ beam)
1	5050.4	35	1024.5	360
2	5178.4	25	1088.5	350
3	5306.4	25	1152.5	200
4	5434.4	25	1216.5	216
5	5562.4	24	1280.5	122
6	5690.4	25	1344.5	88
7	5818.4	26	1408.5	90
8	5946.4	26	1472.5	102
9	6693.4	27	1524.5	151
10	6821.4	22	1588.5	...
11	6949.4	24	1652.5	107
12	7077.4	23	1716.5	102
13	7205.4	23	1780.5	110
14	7333.4	26	1844.5	112
15	7461.4	25	1908.5	120
16	7589.4	27	1972.5	150
1-16	6319.9	6	1498.5	37

the N II/H α–M_B relation given by Kennicutt et al. (2008). We also used H α velocity dispersion data of bright H II regions taken with the scanning Fabry–Perot interferometer on the 1.6m telescope at the Observatoire de Mont Mégantic (OMM, Quebec) in 2012 September. Observing details can be found in Kam et al. (2015). The reduction and calibration of the data cube was performed using the FPREDUC package (Daigle et al. 2006). This pipeline provides tools to calibrate automatically Fabry–Perot data into velocity units, detects and subtracts the continuum from the emission line, and masks out the areas of the galaxy that do not have line emission.

M 33 was observed with the MIPS instrument (Rieke et al. 2004) onboard the *Spitzer Space Telescope* at 24 μm. The basic data reduction and mosaicing were performed with the MIPS instrument Data Analysis Tool version 2.90 (Gordon et al. 2005). The sky and background sources were subtracted as detailed in Tabatabaei et al. (2007a). We also used the far-infrared (FIR) maps taken at 70 and 160 μm with the *PACS* instrument (Poglitsch et al. 2010) onboard the *Herschel space telescope* as part of the Herschel M 33 extended survey open time key project *HerM33es* (Kramer et al. 2010). The *PACS* data were reduced using the scanamorphos algorithm (Roussel 2013), as discussed in detail in Boquien et al. (2011, 2015). The CO(2-1) line emission was observed with the IRAM-30m telescope, as detailed in Gratier et al. (2010) and Druard et al. (2014). The HI-21 cm line was mapped with the *VLA* (Gratier et al. 2010).

All maps used in our analysis were convolved to the resolution of the 1.5 GHz image (∼15 arcsec) and projected to the same grid and centre position. We applied the dedicated convolution kernels provided by Aniano et al. (2011) for the Spitzer/Herschel maps and Gaussian kernels for the rest.

2.3 Short spacing correction

Interferometric observations miss much of the extended structures of the galaxy due to missing short spacings. The VLA observations are insensitive to angular scales larger than $\theta \sim \lambda/B_{min}$ that is ∼ 5′ and 22 arcmin at 6.3 GHz (or 4.8 cm) and 1.5 GHz (or 20 cm), respectively, corresponding to the shortest baselines of $B_{min} \sim 35$ m at C and D configurations. This results in negative bowl artefact around strong sources. For the short spacing correction (SSC), we combined the VLA maps with the Effelsberg single-dish data at corresponding frequencies presented in Tabatabaei et al. (2007b) in the uv plane using the AIPS task 'IMERG'. This program merges two input images by Fourier transforming both, normalizing the second (the lower resolution map) to amplitudes within a uv annulus of the first, then producing an output transform plane consisting of the inner plane from the second input, a combination of the two within the annulus and the outer plane from the first. The output image is the back transform of this merged uv plane[3]. Before running IMERG, the *VLA* and Effelsberg maps were projected into the same geometry and exact frequency (using $\alpha = -0.7$, $S \propto \nu^{\alpha}$, Tabatabaei et al. 2007b), taking into account that the number of pixels in the map must be an integer power of 2 in both axes. The uv range (or min. and max. baselines in kλ) that defines the annular region of assumed overlap between the low- and high-resolution images should be set in this program so that the combined image has (1) an integrated flux density and (2) a distribution of diffuse emission equal/similar to that of the low-resolution single-dish data. At 6.3 GHz, these are achieved using a uv range of 0.739–1.236 kλ. At 1.5 GHz, a few strong sources are subtracted from the *VLA* and Effelsberg maps before merging them to avoid distortion effects caused by them. The uv range adopted to the residual maps is 0.175–0.236 kλ. Those few sources are then re-added to the combined map. The rms noise in the resulting maps are about 12 μJy per 9.″35 at 6.3 GHz and 48 μJy per 15″ beam at 1.5 GHz.

After the SSC, the integrated flux density increases by about 50 per cent at 1.5 GHz. We note that the negative pixels of the VLA map were put to zero before integrating its flux density, otherwise a much higher increase is obtained. At 6.3 GHz, the SSC leads to ≃ 60 per centincrease in the integrated flux density in the inner 18 × 18 arcmin^2 of the galaxy.

3 THERMAL AND NON-THERMAL SEPARATION TECHNIQUE

The radio maps at the frequencies observed here show a mixture of two main radiation mechanisms, the free–free emission from TH electrons $I_\nu^{th}$and the NTH synchrotron emission from relativistic CR electrons (I_{nt}^{th}, i.e. $I_\nu^{obs} = I_\nu^{th} + I_\nu^{nt}$), referring to different origins and source populations, such as H II regions, supernova remnants, background radio galaxies, and diffuse emission, and to the ionized and magnetized ISM. In order to dissect these sources and map the TH and NTH ISM in M 33, we adapt the Thermal Radio Template technique developed by Tabatabaei et al. (2007c), in which the dust optical depth (proportional to dust mass and extinction) is first mapped across the galaxy. Then the H α emission, as the most direct and physically motivated tracer of the free–free emission, is corrected for attenuation by dust. The NTH RC emission can be determined by subtracting from the observed RC the TH radio emission calculated from the de-reddened H α emission. These steps are explained as follows.

3.1 De-reddening the H α emission

To de-redden the H α emission, we first determine the amount of dust that is attenuating the H α photons using the *Herschel PACS* FIR data at 70 and 160 μm following Tabatabaei et al. (2007c). Assuming a

[3]See http://www.aips.nrao.edu/cook.html

modified blackbody radiation, the dust colour temperature T and optical depth at 160 μm, τ_{160} are obtained from the following equations,

$$\frac{I_{70}}{I_{160}} = \frac{\nu_{70}^{\beta}}{\nu_{160}^{\beta}} . \frac{B_{70}(T)}{B_{160}(T)}, \quad (1)$$

$$I_{160\mu m} = B_{160}(T)\,[1 - e^{-\tau_{160}}], \quad (2)$$

where I denotes the observed intensity, $B(T)$ the Planck function, ν the frequency, and β the dust emissivity index. In a detailed study of dust physical properties in M 33, Tabatabaei et al. (2014) showed that β changes across the galaxy from a mean value of $\beta \simeq 1.8 - 2$ in the inner 4 kpc radius of the galaxy to 1.5 and smaller beyond this radius. Hence, we adopted these variations of β using the above equations. The dust optical depth at 160 μm is then converted to that at 6570 Å, i.e. the wavelength of the H α emission, using the dust extinction coefficient per unit mass at the corresponding wavelengths, $\tau_{H_\alpha} = \kappa_{H\alpha}/\kappa_{160\mu m} . \tau_{160} = 2200\,\tau_{160}$ (e.g. Krügel 2003). This interpolation uses a standard dust model and a Milky Way extinction curve with the total/selective extinction ratio of $R_v = 3.1$ (Weingartner & Draine 2001). Studies of the dust extinction curves towards individual sight lines in M 33 show that R_v is similar to that of the Milky Way on average (Wang et al. 2022). The resulting τ_{H_α} varies from 0 to 1 across M 33 with a mean value of $\simeq 0.4$. Therefore, in agreement with our previous study at much lower resolution of 90 arcsec (Tabatabaei et al. 2007c), M 33 is almost transparent for photons with $\lambda \simeq 6560$ Å propagating towards us. For an inhomogenous distribution of dust and ionized gas, only about one-third of the dust present is effectively attenuating the H α photons (Dickinson, Davies & Davis 2003), and hence, the emission received is given by $I = I_0\, e^{-\tau_{\rm eff}}$ with $\tau_{\rm eff} = \frac{1}{3} . \tau_{H\alpha}$. This means that, on average, only about 14 per cent of the H α emission is absorbed by dust in M 33.

Using the full Herschel data set, we presented maps of dust mass and temperature in M 33 by modelling the dust SED (Tabatabaei et al. 2014) at about 40 arcsec angular resolution (resolution of the SPIRE 500 μm data). These products are not used here because their resolution is poorer than the resolutions of the RC maps. We, however, note that the difference in the resulting dust optical depths obtained based on the two methods is less than 10 per cent at 40 arcsec angular resolution.

A more straightforward de-reddening method of the H α emission is the Balmer-decrement-ratio technique, as it does not depend on the dust filling factor along the line of sight and directly measures the attenuation of photons emerging from ionized gas (see e.g. Calzetti et al. 2000; Kreckel et al. 2013; Kouroumpatzakis et al. 2021; Tacchella et al. 2022). We used this method to trace the TH free–free emission in the centre of NGC 1097 for the first time (Tabatabaei et al. 2018). For M 33, this method is not used because the only map of the Balmer line with reliable calibration available is the H α map. Using the MUSE observations of the H α and H β lines in the Magellanic Clouds, Hassani et al. (2022) performed a detailed comparison of the Balmer-decrement-ratio technique with the dust optical depth method explained above. They mapped the fraction of total dust content attenuating the H α emission in these galaxies and showed that, on average, the two methods agree well on scales of giant molecular clouds (GMCs) and larger.

3.2 Mapping the RC components

The radio free–free intensity in mJy beam^{-1}, I_ν^{th}, is related to the brightness temperature T_b in Kelvin through the Rayleigh Jeans relation:

$$I_\nu^{th} = \frac{\theta_i \theta_j}{1.36\lambda^2} T_b, \quad (3)$$

with θ_i and θ_j the beamwidth, along the major and minor axes in arcsec, and λ the radio emission wavelength in cm. In an ionized gas, T_b is related to the H α intensity, $I_{H\alpha}$, in erg cm^{-2} s^{-1} sr^{-1} via

$$\begin{cases} T_b = T_e(1 - e^{-f(T_e)\, I_{H\alpha}}), \\ f(T_e) = 3.763\, a\, \nu_{\rm GHz}^{-2.1}\, T_{e4}^{-0.3}\, 10^{\frac{0.029}{T_{e4}}}, \end{cases} \quad (4)$$

where T_e is the electron temperature in K, T_{e4} is T_e in units of 10^4 K, and taking into account the contribution from singly ionized He. This relation uses the Gaunt factor approximation of Altenhoff et al. (1960) with $a \simeq 1$. In case the ionized gas is optically thin for TH radio continuum (RC) photons, the following relation holds between the intensities of the TH radio and H α emission

$$\left(\frac{I_\nu^{\rm th}}{\rm mJ/beam}\right) = 3.074 \times 10^{-35}\, \theta_i \theta_j\, \nu_{\rm GHz}^{-0.1}\, T_{e4}^{0.668} \times 10^{\frac{0.029}{T_{e4}}} \left(\frac{I_{H\alpha}}{\rm erg\,cm^{-2}\,s^{-1}\,sr^{-1}}\right). \quad (5)$$

The present study is, however, based on the more general condition given by equation (4) adopting an electron temperature of $T_e = 10^4$ K. The resulting TH fraction ($I_\nu^{\rm th}/I_\nu^{\rm obs}$) drops by about 20 per cent, assuming $T_e = 7000$ K (Tabatabaei et al. 2013a). As shown by Tabatabaei et al. (2007c), the TH fraction is by at least a factor of 2 less sensitive to variations in T_e than to variations in the synchrotron spectral index (α_n, $I_{\rm nt} \propto \nu^{\alpha_n}$), assumed to be fixed in the classical separation technique. After mapping the TH intensity, the NTH intensity, $I_\nu^{\rm nt} = I_\nu^{\rm obs} - I_\nu^{\rm th}$, is calculated for each pixel of the maps at 1.5 and 6.3 GHz.

4 RESULTS

4.1 Overall distribution of RC

The maps shown in Fig. 1 illustrate structures emitting RC across the entire disc of M 33 at 1.5 GHz and the inner 18 × 18 arcmin^2 area at 6.3 GHz. While the structures are limited to radio sources before the SSC (left-hand panels), clumps surrounding the bright sources, spiral arms, extended structures, and diffuse emission from the disc are evident only after the SSC (right-hand panels). We now investigate the nature and origin of each RC component.

4.1.1 Radio source population

Before the SSC, we extracted radio sources with scales of giant H II regions and smaller, i.e. <200 pc (57 arcsec), from the observed mosaics at 6.3 and 1.5 GHz using the AIPS source extraction task called *SAD*. The task finds potential islands of emission down to a threshold level in a few rounds of searching. Then each island is fitted by one or multiple elliptical Gaussians (in case of multiple peaks) while allowing the fit to find angular sizes of sources starting with the beam size.

Setting the threshold to 5σ rms, 516 sources were found with peak intensities >200 μJy per 15 arcsec beam at 1.5 GHz (Fig. 1, top-left). At 6.3 GHz, we found 488 sources with a threshold of 35 μJy per 9.35 arcsec (5σ rms) in the inner 18 × 18 arcmin^2 (Fig. 1, bottom-left).[4]

[4]The catalogues at original resolutions and map sizes are presented as an appendix in the electronic version.

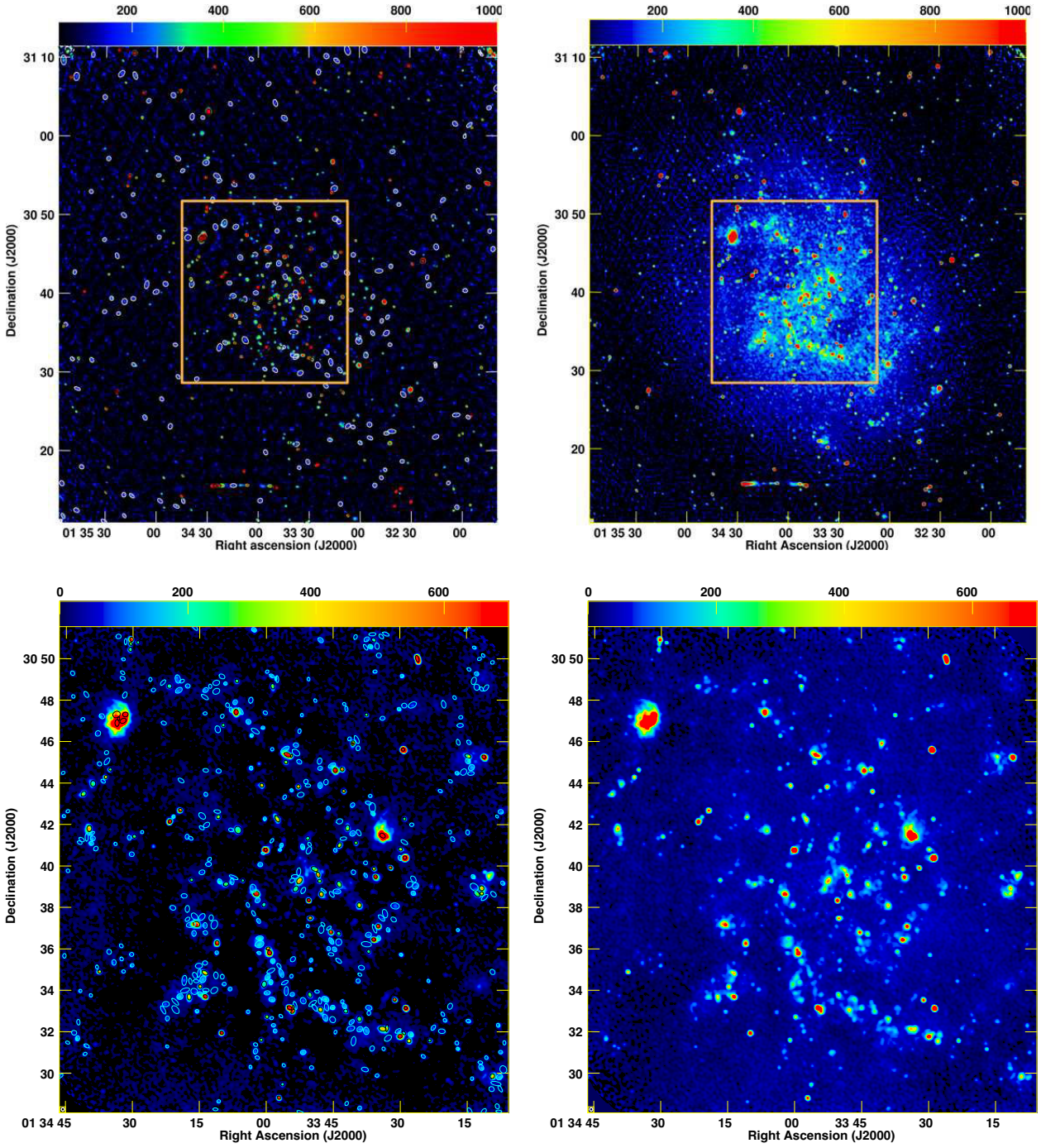

Figure 1. Observed RC emission at 1.5 GHz (*top*) and 6.3 GHz (*bottom*) before (*left*) and after correcting for missing short spacing information (*right*). The angular resolution of 15 arcsec at 1.5 GHz and 9.″35 at 6.3 GHz are shown as circles in the bottom-left corner of each map. In the left-hand panels, the radio sources found at $>5\sigma$ rms are indicated by ellipses (different colours used for a better contrast against background). Angular size and position angle of the sources extracted (see Section 4.1.1) are listed in Tables 5 and 6. Rectangles on top panels indicate the corresponding area observed at 6.3 GHz shown in the bottom panels.

For sources having the beam size or smaller, the peak intensity is taken as the integrated flux density. We note that the number of radio sources found at 6.3 GHz is by a factor of 2.6 larger than that found by Gordon et al. (1999) within 20 arcmin of the centre of M 33.

As the full-spectrum analysis is limited to the C-band observations' field of view, we build a subsample of sources in the inner 18 × 18 arcmin^2 area of M 33. To obtain their 1.5–6.3 GHz spectral index, the 6.3 GHz map is first convolved to the same resolution as the 1.5 GHz map. At this resolution, about 343 sources were fitted at 6.3 GHz with a threshold of 50 μJy (5σ rms), while only about 204 were found in the same area at 1.5 GHz due to this image's lower sensitivity. The results are cross-matched by considering a maximum source separation of half of the L-band synthesized beam. About 167 sources are detected emitting at both 1.5 and 6.3 GHz for which we

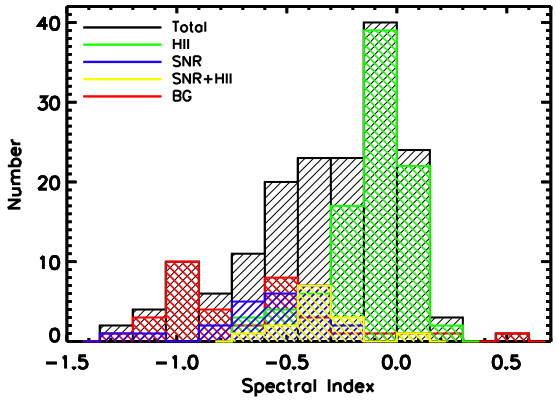

Figure 2. Histogram of the spectral index of radio sources in the inner 18 × 18 arcmin disc of M 33 with >5σ detections at both 1.5 and 6.3 GHz frequencies, which are L and C bands, respectively.

determined the spectral index α ($S \sim \nu^{\alpha}$). We note that it is, of course, possible to build a larger sample by measuring the 1.5 GHz integrated flux densities at the source positions of the more sensitive 6.3 GHz observation. However, to measure the spectral index more robustly, a consistent S/N at different frequencies is required that is taken to be 5σ rms. Table A1 lists the source properties in the inner 18 × 18 arcmin^2 of M 33.

To identify these sources, we first cross-correlated the final sample with catalogues presented by Gordon et al. (1999), Long et al. (2010), and White et al. (2019). These authors classified radio sources mainly using their [S II]:Hα ratios and, when available, characteristics of their X-ray emission (Long et al. 2010; White et al. 2019). Generally, SNRs have higher [S II]:Hα ratios (0.4–1) than H II regions because their radiative shocks contain cooling zones where [S II] is the dominant ionization state of S, whereas in (bright) H II regions, [S III] is the dominant ionization state (Dodorico & Sabbadin 1976; Levenson et al. 1995). From our selected sample of sources, about 51 per cent are found to be known H II regions (three of which emit X-ray as well), 15 per cent SNRs, 8 per cent H II + SNRs, and 15 per cent BG sources. The remaining radio sources have no classified counterparts but some coincide with X-ray sources. We determine a mean radio spectral index of $\alpha = -0.12 \pm 0.16$ for the H II regions (where the error is the standard deviation), a value that agrees with an optically thin TH spectrum ($\alpha \simeq -0.1$). The spectral index is steeper for the combined H II + SNR sources with a mean $\alpha = -0.37 \pm 0.16$. For sources identified as SNRs, we obtain $\alpha = -0.60 \pm 0.30$ and for BGs, $\alpha = -0.65 \pm 0.44$.

We further investigate if the sources classified as unknown in the White et al. (2019) catalogue belong to M 33 or are BG sources. A robust determination of spectral index can help to identify different types of radio sources. As mentioned above, the emission is predominantly free–free in H II regions with a flat spectrum $\alpha \simeq -0.1$. In SNRs, the emission mechanism is synchrotron and the spectral index should be steeper than −0.2. Emission from background radio galaxies is also synchrotron with a spectral index that is often steeper than −0.5. It can, however, be flatter and even inverted for very compact radio sources such as some quasars and other active galactic nuclei due to synchrotron self-absorption (e.g. Kellermann & Owen 1988). Cross-correlation with Hα emission can provide additional constraints for the internal sources as the Hα line emission from BG radio sources is unlikely to fall in the velocity window adopted for M 33. From the 18 unknown sources that have spectral index information, seven sources coincide with Hα sources. Their relatively flat spectral index with a mean $\alpha = -0.29 \pm 0.30$ makes them candidates of H II regions (or H II + SNRs) in M 33. Eleven sources are taken as external to M 33, increasing the total number of BGs to 36. We note that this addition does not change the BGs' mean α (=-0.65 ± 0.44). Fig. 2 shows a histogram of the spectral index α of the different source types.

4.1.2 *Diffuse disc and extended RC emission*

The extracted sources account for 34 per cent of the 1.5 GHz emission and 44 per cent of the 6.3 GHz emission from the inner 18 × 18 arcmin^2 of M 33. The remaining emission emerges from patches of extended structures (on scales of <2 kpc), surrounding star-forming regions in spiral arms (photo-ionized or shocked-ionized regions) or from structures in between the arms (likely of NTH origin, see Section 4.2). On larger scales, the general diffuse disc of the galaxy can contribute significantly. Hence, to determine the relative contribution of the extended structures, the contribution from the diffuse disc must be subtracted. The surface brightness of spiral galaxies generally falls exponentially with galactocentric radius R, with an exponential scale length l. For the full disc of M 33, the scale lengths of the RC emission are presented by Tabatabaei et al. (2007b) at different frequencies.[5] The sky-plane projection of the diffuse RC disc is described as $I_{\rm d}(R) = A\,exp(-R/l)$, with R the galactocentric radius. After removing the point sources, we fit this model to only diffuse regions in interarm regions and/or outer parts to avoid contributions from other extended structures. The model parameters, A and l, are obtained using the bisector least-squares fit (Isobe et al. 1990) at different frequencies (Table 7).

Subtracting the diffuse disc, we then separately map the extended structures. An example of this structural decomposition is shown in Fig. 4 for the RC emission at 6.3 GHz. The integrated flux density and contribution of diffuse disc and extended structures in the inner part of M 33 are then determined (Table 7). The integrations are performed in rings in the plane of the galaxy around the centre out to a radius of 12′.75 after subtracting the background radio sources.

The uncertainties in the integrated flux densities are determined taking into account the map fluctuations ($\delta_{\rm rms} = \sigma_{\rm rms}\ \frac{a}{\theta}\ \sqrt{\frac{\rm N}{1.133}}$, with $\sigma_{\rm rms}$ is the rms noise level, θ the angular resolution, N the number of pixels, and a the pixel size), calibration uncertainty ($\delta_{\rm cal} \simeq 3$ per cent for the VLA, and 2 per cent and 5 per cent at 1.5 and 6.3 GHz, respectively, for the Effelsberg observations), and the uncertainty of the baselevel in the single-dish map ($\delta_{\rm base} = \sigma_0\ {\rm N_{beam}}$ with σ_0 the baselevel uncertainty of the Effelsberg map $\sigma_0 \simeq 0.2\ \sigma_{\rm rms}$). Hence, the total uncertainty is given by $\delta = \sqrt{\delta_{\rm cal}^2 + \delta_{\rm rms}^2 + \delta_{\rm base}^2}$. The errors in the integrated flux density of the maps are then propagated to obtain uncertainties in the ratios reported in Table 7.

At 6.3 GHz, most of the RC emission emerges from unresolved sources (46 per cent ± 2 per cent), while the diffuse disc dominates at 1.5 GHz (41 per cent ± 3 per cent). The contribution of the extended structures to the total RC is about 23 per cent and 18 per cent at 1.5 and 6.3 GHz, respectively.

4.2 Structure of TH and NTH emission

The radio source populations of M 33 were described in Section 4.1.1. The natures of the diffuse and extended components are, however,

[5]Exponential fits to the new VLA data lead to similar scale lengths at corresponding galactocentric radii.

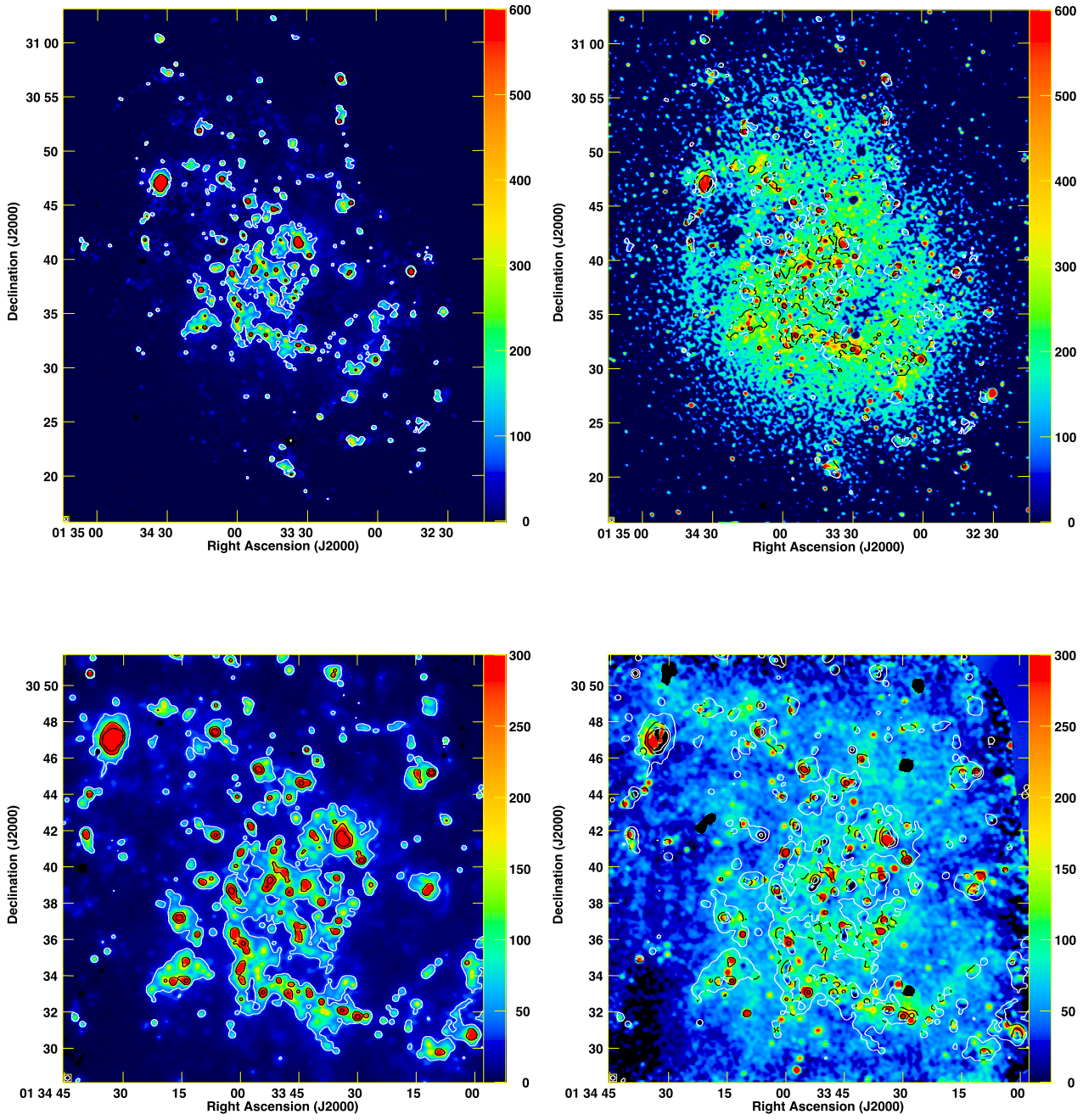

Figure 3. Top: the TH (left) and NTH (right) RC emission in μJy beam^{-1} at 1.5 GHz overlaid with contours of the TH free–free emission at levels 70 and 500 μJy beam^{-1}. Bottom: same as above at 6.3 GHz overlaid with the TH emission contours at levels 40, 200, and 600 μJy per beam^{-1}. The maps at 6.3 GHz cover only the inner 18 × 18 arcmin^2 galaxy. The half power beamwidth of 15 arcsec is shown by a circle in the left corner of each image. Background radio sources with peak intensities of ≥4.6 mJy beam^{-1} at 1.5 GHz (≥1 mJy beam^{-1} at 6.3 GHz) are subtracted from the NTH maps. Negative NTH intensity in some parts of bright HII regions can be linked to local variations in the electron temperature and/or the N II-to-H α ratio causing an over-prediction of the TH emission.

uncertain. It is unclear what physical processes shape the observed extended features: are they part of the gas ionized through TH processes or are they highlighting relativistic particles travelling in the magnetized ISM? How much of this magnetized ISM is coupled with the neutral gas? Mapping the TH and NTH components of the RC emission is the first step towards addressing these questions. As explained in Section 3.2, the decomposition is performed at 6.3 GHz (12[6] and 15 arcsec) and 1.5 GHz (15 arcsec resolution). The resulting maps are shown in Fig. 3 at 15 arcsec resolution. Various structures are visible in the TH and NTH maps, with some similarities and

[6]Resolution is limited by the 160 μm PACS data used to estimate the dust extinction (see Section 3.1).

Table 5. Radio sources detected in M 33 at 1.5 GHz (the full table is available as supplementary material). Parameters Maj, Min, and PA refer to the deconvolution of the best-fitting major axis, minor axis, and position angle, respectively.

ID	Peak flux density μJy beam^{-1}	Integrated flux density μJy	RA (^{h} ^{m} ^{s})	Dec. ($^{\circ}$ $'$ $''$)	Maj arcsec	Min arcsec	PA deg.
1	183 ± 41	558 ± 162	01^{h}31^{m}38^{s}.08	31°06′00″.85	27.4 ± 6.2	25.1 ± 5.7	110 ± 105
2	249 ± 44	290 ± 85	01^{h}31^{m}39^{s}.08	30°11′56″.87	20.5 ± 3.7	12.8 ± 2.3	177 ± 15
3	368 ± 41	1028 ± 152	01^{h}31^{m}39^{s}.28	30°10′49″.94	12.9 ± 0.9	10.7 ± 0.8	41 ± 16
4	1081 ± 42	2610 ± 140	01^{h}31^{m}39^{s}.70	31°10′09″.06	30.2 ± 1.2	18.0 ± 0.7	11 ± 3
5	1319 ± 43	2400 ± 110	01^{h}31^{m}41^{s}.13	31°10′21″.43	22.7 ± 0.7	18.0 ± 0.6	154 ± 6
6	249 ± 43	354 ± 96	01^{h}31^{m}41^{s}.15	30°45′35″.83	19.3 ± 3.4	16.5 ± 2.9	169 ± 46
7	933 ± 45	1050 ± 84	01^{h}31^{m}41^{s}.48	30°49′23″.76	16.6 ± 0.8	15.3 ± 0.7	54 ± 23

Table 6. Radio sources detected in the inner 18 × 18 arcmin^2 M 33 at 6.3 GHz (the full table is available as supplementary material). Parameters Maj, Min, and PA refer to the deconvolution of the best-fitting major axis, minor axis, and position angle, respectively.

ID	Peak flux density μJy beam^{-1}	Integrated flux density μJy	RA (^{h} ^{m} ^{s})	Dec. ($^{\circ}$ $'$ $''$)	Maj arcsec	Min arcsec	PA deg.
1	62.7 ± 10.8	78.20 ± 21.7	01^{h}33^{m}06^{s}.64	30°31′28″.17	12.3 ± 2.1	8.8 ± 1.5	4 ± 21
2	37.2 ± 9.9	183.1 ± 58.0	01h33^{m}06^{s}.89	30°30′11″.02	22.4 ± 5.9	19.3 ± 5.1	29 ± 72
3	142.7 ± 10.5	224.97 ± 25.07	01h33^{m}06^{s}.95	30°10′10″.42	12.9 ± 0.9	10.7 ± 0.8	41 ± 16
4	134.6 ± 10.3	293.6 ± 31.1	01h33^{m}07^{s}.38	30°42′37″.12	14.7 ± 1.1	12.97 ± 0.99	79 ± 24
5	124.3 ± 10.7	169.1 ± 22.9	01h33^{m}07^{s}.48	30°31′00″.96	11.4 ± 1.0	10.4 ± 0.9	87 ± 38
6	41.4 ± 10.3	85.4 ± 29.9	01h33^{m}07^{s}.59	30°29′14″.87	20.1 ± 5.0	8.9 ± 2.2	31 ± 11
7	171.2 ± 10.1	526.9 ± 40.0	01h33^{m}07^{s}.76	30°29′49″.41	18.3 ± 1.1	14.7 ± 0.9	128 ± 11

Table 7. Contribution of diffuse disc, extended emission, and discrete sources to the total integrated flux density in the inner 18 × 18 arcmin^2 area of M 33 for the observed RC and its TH and NTH components. The five brightest background sources are excluded. The parameters a and b are the diffuse disc model fit parameters in $Y = b\,X - A$ with $Y = ln(I_d)$, $X = R$, $A = ln(a)$, and $b = 1/l$.

ν (GHz)	Component	S_{total} (mJy)	S_{disc}/S_{total}	$S_{extended}/S_{total}$	S_{source}/S_{total}	a (μJy beam^{-1})	b (kpc)$^{-1}$
1.5	Observed	812 ± 68	0.41 ± 0.03	0.23 ± 0.02	0.36 ± 0.02	118 ± 3	0.18 ± 0.02
	NTH	610 ± 60	0.44 ± 0.03	0.26 ± 0.02	0.30 ± 0.02	101 ± 4	0.16 ± 0.02
	TH	202 ± 10	0.30 ± 0.02	0.15 ± 0.01	0.55 ± 0.02	24 ± 3	0.49 ± 0.06
6.3	Observed	432 ± 29	0.36 ± 0.03	0.18 ± 0.02	0.46 ± 0.02	71 ± 10	0.32 ± 0.09
	NTH	257 ± 19	0.40 ± 0.03	0.20 ± 0.02	0.40 ± 0.02	51 ± 2	0.27 ± 0.01
	TH	175 ± 8	0.30 ± 0.02	0.15 ± 0.01	0.55 ± 0.02	21 ± 3	0.49 ± 0.06

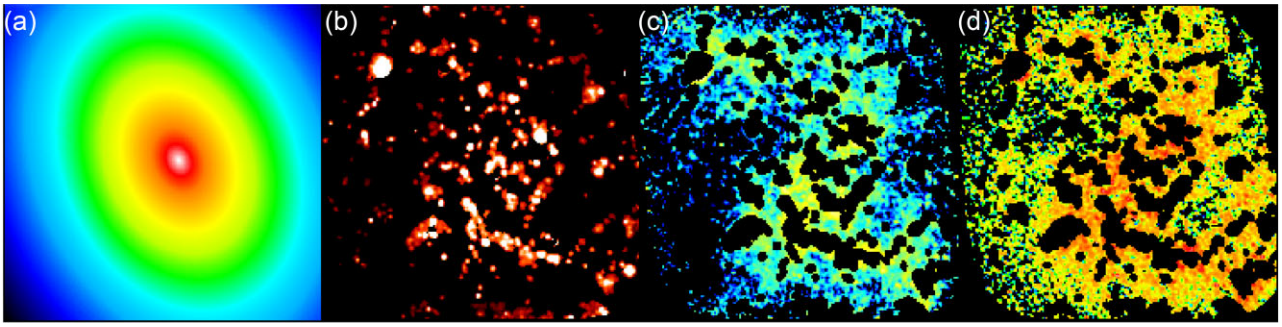

Figure 4. Structural decomposition of the RC emission from the inner 18 × 18 arcmin^2 part of M 33: *a*- diffuse disc, *b*- sources, and *c*- extended structure at 6.3 GHz. The field of view is the same as Fig. 3 (bottom panels). Strong BGs are subtracted, hence, the sources indicate mostly the star-forming regions. Also shown is the extended emission at 1.5 GHz from the same area as of the 6.3 GHz extended emission (*d*). A quantitative comparison of the relative contribution of each structural component at different frequencies is shown in Table 7.

differences depending on the frequency. The most striking difference occurs at 1.5 GHz on larger scales due to the diffuse NTH emission, while there are some agreements on small scales. In particular, giant star-forming regions host both TH and NTH emission, the latter in the form of SNRs and NTH substructures, although the TH and NTH peak intensities can be offset from each other. At 6.3 GHz, the diffuse NTH emission is less extended than at 1.5 GHz: it is more localized and shows a tighter correlation with the TH emission in